Chapter 20
Effect of Re-normalizing and Re-tempering on Inter-critical Heat Affected Zone(S) of P91B Steel

Modassir Akhtar, Akhil Khajuria, and Raman Bedi

Abstract The novel perspective of this paper was to restore the grain boundary (GB) hardening effect in inter-critical heat affected zone (ICHAZ) of boron modified P91 steel (P91B). To achieve this, samples of the base metal (BM) of P91B steel were thermally simulated by Gleeble followed by post-weld heat treatment (PWHT) and were further re-normalized and re-tempered. With such heat treatment, four different ICHAZ(s) were reproduced. These ICHAZ(s) were subjected to impression creep testing. As impression creep testing brings local deformation, the suitable characterization technique was electron back scatter diffraction (EBSD) for in-depth investigations of microstructural deformation. High creep deformation was observed for simulated ICHAZ followed by PWHT-ICHAZ due to GB softening. Whereas, the least deformation was observed for re-normalized and re-tempered ICHAZ(s) restoring GB hardening. In this respect, type IV cracking was avoided by re-normalizing and re-tempering in P91B steel. This phenomenon was further correlated with the impression creep curves of each ICHAZ with BM.

Keywords Boron modified P91 steel · ICHAZ · Grain boundary hardening and softening effect · Impression creep

M. Akhtar (✉)
Department of Metallurgical and Materials Engineering, National Institute of Technology Warangal, Warangal 506004, Telangana, India
e-mail: amodassir@student.nitw.ac.in

M. Akhtar · A. Khajuria
Department of Materials Engineering, CSIR—National Metallurgical Laboratory, Jamshedpur 831007, India

R. Bedi
Department of Mechanical Engineering, Dr B. R. Ambedkar National Institute of Technology Jalandhar, Jalandhar, Punjab 144011, India

Nomenclature

EBSD   Electron back scatter diffraction
GB   Grain boundary
ICHAZ   Inter-critical heat affected zone
HAGB   High angle grain boundary
HAZ   Heat affected zone
LAGB   Low angle grain boundary
MCR   Minimum creep-damage rate
PWHT   Post-weld heat treatment

20.1 Introduction

P91 ferritic/martensitic steel has superior creep resistance and corrosion resistance that leads to its maximum usage in the form of high temperature and high pressure piping material in nuclear and thermal power plant industries [1, 2]. To obtain leak proof joints majorly that transfers steam, high heat input fusion welding processes such as submerged arc welding, manual metal arc welding, gas tungsten arc welding, etc., are used for fabrication of P91 steel components [3]. As these welding processes bring a narrow width of heat affected zone (HAZ) depending upon thermal gradient and phase transformation experienced, this practice has become a grievance issue due to the manifestation of type IV failure at outer HAZ [4, 5]. In a previous attempt, an effort was given to find type IV region by exclusively reproducing singular HAZs using Gleeble thermal simulation and the study confirmed ICHAZ as type IV region due to the formation of fine and soft grains, coarsening of $M_{23}C_6$ carbides, and recovery of martensitic substructure [6, 7]. Followed by welding, PWHT of P91 weldments is a recommended procedure to curtail both solidity and microstructural heterogeneity across HAZ [8, 9]. During PWHT, dynamic recovery and recrystallization occur at ICHAZ [8]. Subsequently, this microstructure receives an additional preferential recovery and recrystallization of ferritic lath structure during in-service exposure [9, 10].

These problems can be overcome by controlling alloying additions. The addition of carbon in P91B steel stabilizes austenite, which would ease in delaying the formation of delta ferrite. Its addition increases tensile strength, hardness, and hardenability. However, the carbon in P91B steel would promote $M_{23}C_6$ and MX precipitation. But, the high concentration of carbon coarsens these precipitates leading to a reduction in creep strength. The controlled addition of carbon in P91B steel maintains toughness and weldability [11–13]. The addition of chromium is beneficial in P91B steel in improving creep strength and to retain oxidation resistance at elevated temperature. It also forms carbides ($M_{23}C_6$ precipitation), decreases martensitic start temperature, and increases A_{c1} temperature (ferrite stabilizer). High diffusion coefficient of Cr than Mo results in the coarsening of $M_{23}C_6$ carbides [11, 12, 14–18]. While

the addition of Mo in P91B steel stabilizes ferrite (increases A_{c1} temperature) at high-temperature by raising the binding force and favors carbides formation. Similar to Cr, its addition also enhances creep strength and toughness by both preventing graphitization and inhibiting temper embrittlement. It decreases martensitic start temperature (Ms) but improves pitting corrosion resistance. Its concentration more than 1% accelerates $M_{23}C_6$ coarsening and laves phase precipitation by decreasing solid solution strengthening. Mo is also known for providing better hardenability and secondary hardening due to carbide formation during tempering. [11, 12, 14, 16, 17].

Similar to previous, vanadium and niobium are ferrite stabilizers, and carbide and nitride are formers. Formation of these vanadium and niobium phases helps in retaining fine subgrains. But, due to chromium diffusion, niobium carbo-nitrides transform into Z-phase, i.e., Cr[Nb(C,N)] [12, 14, 15]. In contrast to previous, nitrogen is an austenite former, which causes a delay in delta ferrite formation. Its addition promotes nitrides causing better hardenability. Nitrogen also provides solid solution hardening and segregates to dislocation to delay its motion at both high and room temperature. High nitrogen contents (>0.2%) cause both formations of unwanted Z-phase with Cr and porosities in the mould. It also lowers Ms temperature and gives resistance to pitting corrosion [12, 15, 17]. Mn does not provide enough solid solution strengthening and is the cheapest carbide former. It lowers A_{c1} temperature hence austenite stabilizer. Its addition delays carbides separation with M_6C precipitation but promotes $M_{23}C_6$ coarsening by partitioning. Mn is a deoxidant and behaves as sulfur segregation preventer by forming MnS, which promises sound weld deposits. This sulfur in addition to phosphorous promotes hot shortness in the free form at service and processing temperature hence must be kept under ppm. Increased Mn contents may cause temper embrittlement resulting in a loss in creep strength, but gain in hardenability [12, 14, 15, 17, 19].

Controlled addition of silicon stabilizes ferrite and delays lave phase formation resulting in better high-temperature mechanical properties. It improves oxidation resistance and graphitizes carbides by accelerated carbon diffusivity. This accelerated carbon diffusivity promotes $M_{23}C_6$ coarsening [12, 14, 15, 17, 18, 20]. Aluminium graphitizes carbides and in small quantities provides both improved mechanical strength and high-temperature oxidation and corrosion resistance. It is a deoxidant to clean steel, which results in enhanced toughness [14, 17, 19]. Ni graphitizes the carbides that cause a delay in the carbides separation and lowers A_{c1} temperature (austenite stabilizers). In small quantities, it provides better mechanical properties but lowers the ductile to brittle transition temperature. Its addition increases diffusion coefficient (i.e., $M_{23}C_6$ coarsening) but gives corrosion resistance in sulfuric acid [13, 15, 17].

In controlled concentrations, boron enhances creep strength, tensile and creep ductility, and quench hardenability by retaining fine subgrains. The fine grain and stable microstructure in P91B steel are due to its memory effect before and after welding. The decreased self-diffusion coefficient in P91B steel due to its addition delays coarsening of $M_{23}C_6$ carbides and refines MX type carbides/carbo-nitrides, which lead to the occupation of free boron in vacancies of GBs and in lattice site of $M_{23}C_6$ carbides. Such phenomenon promotes the formation of $M_{23}(C,B)_6$ carbides

at GBs and sub-GBs, which are responsible for a decrease in impact toughness and stabilization of ferrite/martensite matrix against both re-austenization during phase transformation and recovery during an early stage of tertiary creep. Boron is known for enhanced GB and sub-GB cohesion due to its segregating nature to these boundaries. These cohesions are mainly responsible for GB and sub-GB strengthening. But the addition of high amount of boron causes hot shortness, GB embrittlement, and intergranular embrittlement. Higher concentration of boron and nitrogen causes the formation of intermetallic phase, i.e., boron nitride, which depletes beneficial effect of boron [12, 14, 15, 17, 21–23].

Our previous studies also revealed a delay in type IV failure on modification of 100 ppm boron in P91 steel at ICHAZ [8, 24–27]. However, the role of all other elements is now clear, but the role of boron is still mysterious in coming to its true mechanism. It was reported that after PWHT, re-normalizing followed by re-tempering may alter type IV failure in P91 steel weldments [3]. However, continuous reports of weldment failure by type IV in boron-free P91 steel being treated by re-normalizing and re-tempering reduced research concentration on this side [28, 29]. Hence, no literature is available that describes phenomenological behaviour for 100 ppm boron added weldments being re-normalized and re-tempered after PWHT. Conventional uniaxial creep testing requires both longer testing time and bulk materials. However, the impression creep testing with flat indenter calls lower testing time and less material [6]. The main advantage of such testing is that it is highly sensitive to minor alloy modification and change in heat treatment [7]. But, the deformation produced by this technique is localized and require special microscopy technique to characterize. EBSD is one of those techniques, which locally characterizes the change in microstructure. However, the laboratory X-ray diffractometer scans bulk surfaces, while characterization through transmission electron microscopy is tedious and unreliable due to poor statistics and difficulty in identifying local substructure. Bearing all points, this paper deals to illuminate softening and hardening effects in ICHAZ during as-simulated, PWHT, and re-normalized and re-tempered conditions due to the presence of miraculous element boron in P91 steel.

20.2 Material and Methods

20.2.1 Material and Heat Treatment History

A 100 ppm boron modified P91 steel was received in normalized and tempered conditions. Its chemical composition and the history of heat treatments are shown in Table 20.1.

Table 20.1 Chemical composition and heat treatment history of as-received P91B steel

Elements	C	Cr	Mo	Mn	Si	V	Nb	Al	Ni	B	N	Fe	Normalizing	Tempering
wt.%	0.10	8.26	0.88	0.33	0.3	0.19	0.06	0.03	0.01	0.01	0.004	Bal.	1050 °C/0.5 h	760 °C/3 h

20.2.2   Physical Simulation of Inter-critical HAZ(s) and Their Re-Normalizing and Re-Tempering Treatments

The purpose of physical simulation of inter-critical HAZ(s) by Gleeble in vacuum was to optimize the process parameters of welding. The sample having a shape of rectangular prism with dimensions 78 mm × 11 mm × 11 mm was used for simulation purpose. The cycle of inter-critical HAZ(s) was consisted of linear heating it from room temperature to inter-critical temperature, i.e., between A_{c1} and A_{c3} temperature. In this temperature, both BCC and FCC phases were present. After reaching to inter-critical temperature range, it was soaked for 8 s and ultimately cooled according to Eq. 20.1. Equation 20.1 is used for exponential cooling. However, the definition and selection of inter-critical HAZ(s) were based on its conventional definition same as reported earlier [6–8, 10]. Four ICHAZ samples were physically simulated at heating and cooling rates of 40 °C and 20 °C, respectively, at the peak temperature and soaking time of 865 °C and 8 s, respectively. First condition, i.e., as-simulated ICHAZ is referred to as ICHAZ. Further, second ICHAZ sample in as-simulated condition was exposed to PWHT at 760 °C/3 h followed forced air cooling and is referred to as 760ICHAZ. Third sample after both simulation and PWHT was re-normalized at 1050 °C/0.5 h followed by re-tempering at 760 °C/2 h and is referred to as 6ICHAZ. Only one sample after re-normalizing and re-tempering was air cooled, i.e., 6ICHAZ. At last, fourth sample, which was not air cooled and was further exposed to 800 °C/2 h and is referred to as 7ICHAZ. Such heat treatments of ICHAZ(s) with heat treatment of BM are shown in Fig. 20.1.

$$T = T_{\mathrm{P}} \times \exp(-0.47t/\Delta t) \qquad (20.1)$$

where T is instantaneous temperature in °C, T_{p} is peak temperature in °C, t is time in seconds, and Δt is time to cool from 800 to 500 °C in seconds. The heat input
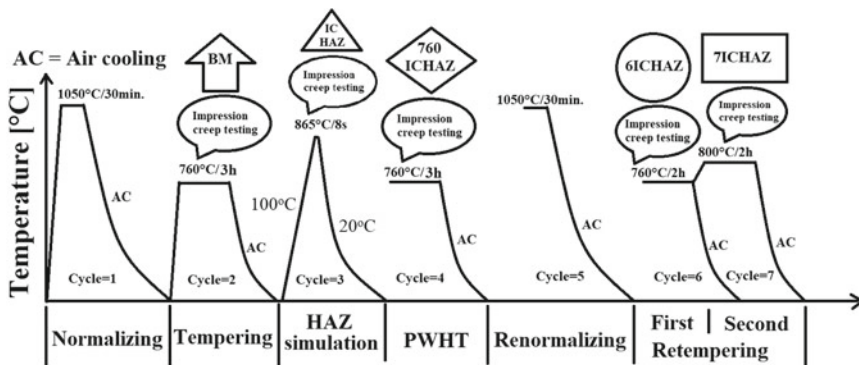

Fig. 20.1 Thermal history of P91B steel from as-received state to re-normalized and re-tempered state

experienced during the simulation was 1.6 kJ/mm, which was found using a real-time data acquisition system during submerged arc welding.

20.2.3 Impression Creep Testing

After completion of simulation of ICHAZ(s) and further heat treatments, samples from each condition were exposed to impression creep testing at an operating temperature of 625 °C and applied stress of 350 MPa. The impression creep testing was done for random time periods for all samples till minimum creep-damage rate (MCR) was obtained, just after the primary creep stage in each condition on the polished surface (polished up to 600 grit emery paper). Since high temperature causes the formations of Cr_7O_6 and $Cr_{23}O_6$ on sample surface, which may hinder to deform sample in compressive loading; therefore, the creation of vacuum in the order of 10^{-3} mbar was mandatory inside the chamber. The dimensions of the sample were $10 \times 10 \times 10$ mm^3 for impression creep testing. Impression creep testing considers compression type loading, which makes it mandatory to adopt a correlation factor to convert compressive stress of impression creep testing into tensile stress of uniaxial creep testing. This conversion factor was reported for many materials as 3.3 and can be compared with the ratio of hardness by its strength [30, 31]. In this respect, the compressive load (350 MPa) used in this paper would correspond to 106 MPa in tensile stress conditions. Linear variable differential transducer was used to obtain the values of depth of impression with respect to time during impression creep testing. For getting impression velocity to distinguish primary and secondary creep stage during impression creep testing, the values obtained from linear variable differential transducer, i.e., depth of impression were differentiated with respect to time. Subsequently, the impression velocity at the end of secondary stage creep was used to obtain MCR. The governing equations used to calculate stress, impression velocity, and MCR are given in Eqs. 20.2, 20.3, and 20.4 [7, 26, 31, 32].

$$\text{Stress} = \frac{4F}{\pi d^2} \tag{20.2}$$

$$\text{Impression velocity} = \frac{\text{d(depth of impression)}}{\text{d}\tau} \tag{20.3}$$

$$\text{Minimum creep-damage rate} = \frac{\text{Impression velocity}}{\beta d} \tag{20.4}$$

where F is applied load in Newton, d is the diameter of indenter (1.5 mm) and the material was made up of tungsten carbide, τ is test time in seconds and β is the correlation factor (~1). Yu and Li reported this value of β to correlate the impression creep data and uniaxial tensile creep data by the finite element method [33]. After Yu and Li [33], this value has been used to relate both the creep testing for many materials [7, 26, 34–36].

20.2.4 Electron Back Scatter Diffraction

After impression creep testing, for EBSD characterization, samples were mechanical polished up to 1200 grit energy paper followed by electro-chemical polishing in the solution of 20% perchloric in methanol at 14–16 V for 5 s. EBSD measurements were done at deformed zone at a step size of 100 nm for $100 \times 100 \ \mu m^2$ surface area. The orientation data obtained from EBSD was processed in TSL–Orientation Imaging Microscopy 7 software.

20.3 Results and Discussion

20.3.1 Creep Deformation of ICHAZ(s) Under Different Heat Treatment Conditions

Impression creep testing results of ICHAZs are shown in Fig. 20.2 in terms of depth of impression as regards BM of P91B steel. Depth of impression of BM exhibited a sharp transition between primary and secondary creep deformation (as indicated by arrow) followed by 6ICHAZ and 7ICHAZ. While the relatively smooth transition was observed for ICHAZ and 760ICHAZ samples in Fig. 20.2a. Figure 20.2b shows primary and secondary impression velocity of all samples. It can be noted in Fig. 20.2a that longer primary impression velocity was obtained for 6ICHAZ followed by BM, 7ICHAZ, 760ICHAZ, and ICHAZ. This phenomenon signified the strain hardening capability of samples in the descending order, which was equilibrated with creep damage after primary impression velocity. Equilibrium strain hardening with creep deformation in terms of MCR was plotted (Fig. 20.3).

The term microstructural degradation comes when there are undesirable changes in microstructural features like coarsening of precipitates and subgrains, formation
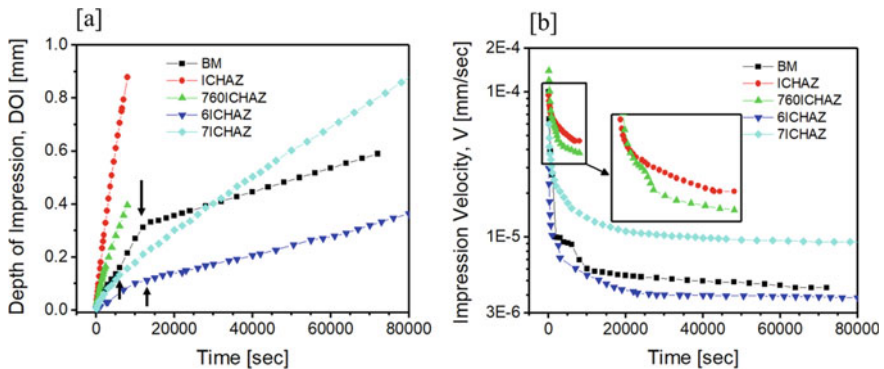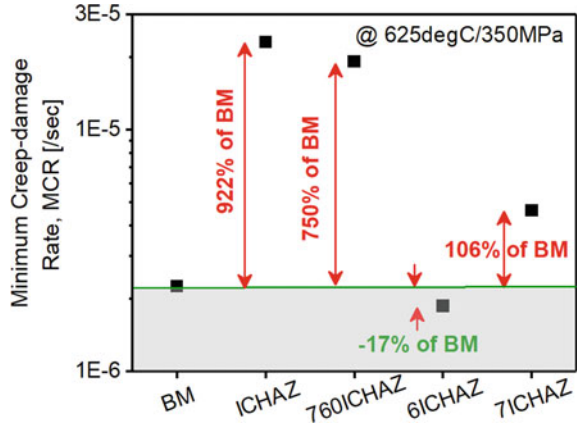

Fig. 20.2 Depth of impression and impression velocity of ICHAZs as regards BM of P91B steel

Fig. 20.3 Percent change in MCR of ICHAZ(s) as regards MCR of base metal

and growth of intermetallics by depleting solid solution from the matrix, etc. In impression creep testing, the degradation of microstructures may or may not occur depending upon chemical composition, heat treatment history, prior loading conditions, operating temperature, and applied load. In contrast to previous, creep damage comes due to the formation of creep cavities during the tertiary creep stage of tensile creep testing. In this testing, high accumulation of vacancies caused the formation of creep voids, which finally agglomerate to form creep cavities under tensile loading. But, during impression creep testing, an absence of tertiary creep stage caused a handicap in the formation of creep cavities. An application of compressive loading during impression creep testing, suppresses not only the tertiary creep stage but also reduces the availability of free vacancies to provide GB sliding, which is truly responsible for the failure of a component. Here, the key link between two-creep testing to use term creep damage is the manipulation of the number of available vacancies, which is essential to accommodate creep testing either in tensile loading and creep loading. Therefore, the term creep damage is also applicable for impression creep.

As observed from Fig. 20.3, MCR of BM was assumed as a reference value to understand the softening and hardening phenomena of GB onset from different heat treatment conditions. High GB hardening around more than 17% from BM was observed for 6ICHAZ followed by 7ICHAZ (106% weaker than BM). Whereas, high GB softening was observed in ICHAZ (around 922% of BM) followed by 760ICHAZ (around 750% of BM). Based on the Monkman–Grant relationship reported in [1], the ratio of creep life for BM: ICHAZ: 760ICHAZ: 6ICHAZ: 760ICHAZ was 1: 0.004: 0.01: 1.05: 0.4, respectively. Hence, it can be said that GB softening during impression creep testing in ICHAZ and 760ICHAZ caused 99.6% and 99% reduction in creep life as regards BM. Whereas, GB hardening during impression creep testing improved creep life for 6ICHAZ and 7ICHAZ as regards both simulated and PWHT treated ICHAZs. But, the creep life in 7ICHAZ decreased as regards creep life of BM by 60%, whereas the creep life of ICHAZ increased by 5% as regards creep life of BM.

20.3.2 EBSD Measurements of ICHAZ(s) Under Different Heat Treatment Conditions

20.3.2.1 Boundary Density

Ferritic/martensitic 9% Cr steels derive their creep strengths from various strengthening mechanisms that simultaneously occur to retard dislocation motion during creep exposure. Martensitic recovery in these grades becomes cumbersome on the application of thermal load since dislocations have to cross number of obstacles in their path like GBs/sub-GBs, precipitates, and solute atoms in solid solution or dislocations themselves. In this respect, GBs/sub-GBs act as barriers to the movement of dislocations across them, which contribute to this type of hardening mechanism in 9Cr steels. Therefore, an increase in the fraction of boundaries in microstructure creep strength can be improved, since small boundaries, i.e., sub-GBs would serve better to hinder the motions of dislocations in them. The sub-GBs are usually low angle grain boundaries (LAGB), whereas GBs are high angle grain boundaries (HAGB). With the application of EBSD technique, LAGB and HAGB can be distinguished based on specified misorientation angles.

Figure 20.4 shows the plot of boundary line per unit area versus misorientation angle, which is referred to as GB density. It can be observed that low angle grain boundary, i.e., 0°–15° (LAGB) does not exhibit much variation among ICHAZ, 760ICHAZ, and 6ICHAZ as the lath block structures were similar whereas it increased for 7ICHAZ. This was attributed to high tempering temperature for long time, which led to recrystallization of lath block structure. However, boundary density as regards high angle grain boundary, 15°–63° (HAGB) was higher in 7ICHAZ followed by ICHAZ while similar values of boundary density were observed for 760ICHAZ and 6ICHAZ.

Fig. 20.4 Boundary line per unit area versus misorientation angle
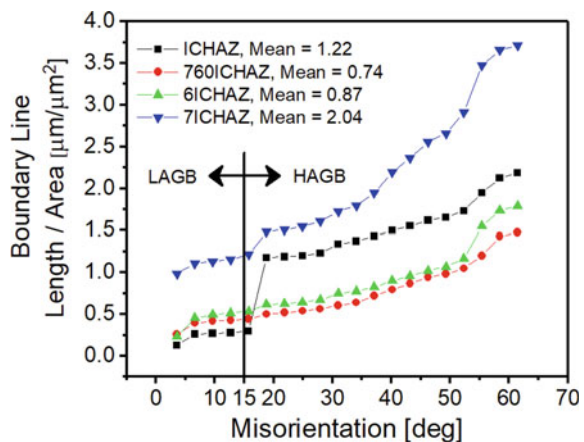
20.3.2.2   Grain Orientation Spread

The formation of dislocations in a material is indicated from the residual strain that occurs as local variations in the microstructure. To distinguish these strain variations, EBSD grain orientation spread parameter can be used. This method provides the same value to each scanned point within a single grain. Therefore, based on different strain values of different grains, variation in microstructural strain could be analyzed. Such an approach has been implemented to distinguish the recrystallized grain fraction, sub-structured grain fraction, and deformed grain fraction in P91 steel (Fig. 20.5, Table 20.2) [29, 37]. In this respect, Gleeble simulated and deformed ICHAZ showed higher recrystallization having no deformed grains. This recrystallization of ICHAZ
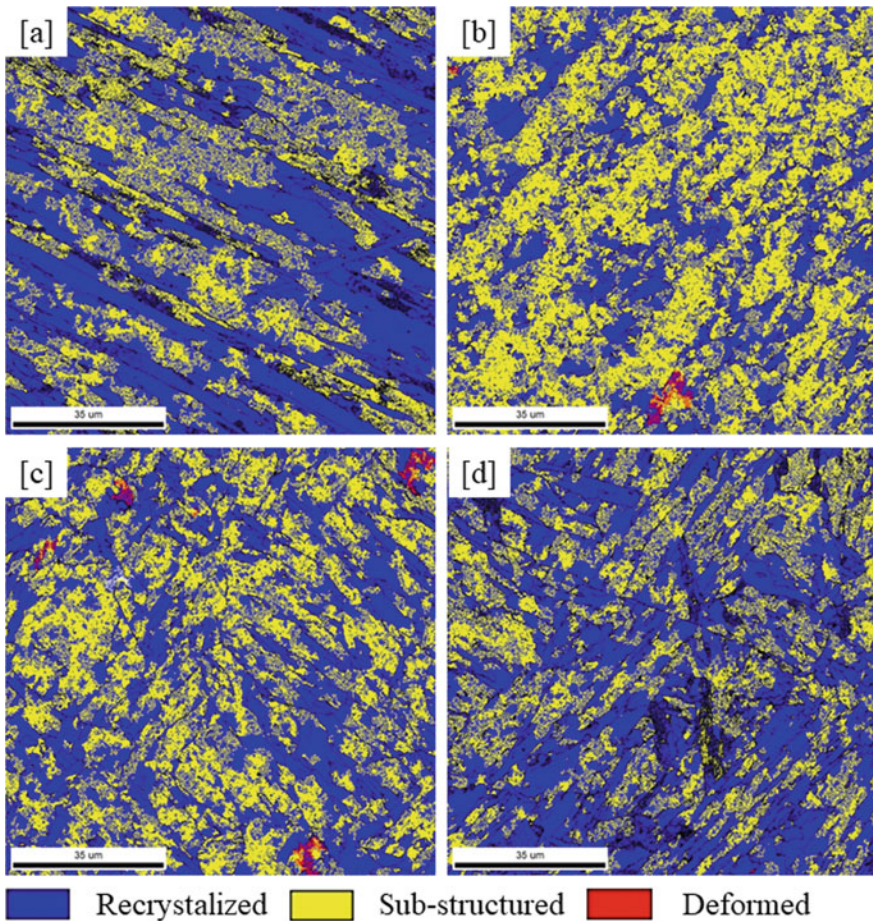

Fig. 20.5   Grain orientation spread showing recrystallized, sub-structured, and deformed grains of **a** ICHAZ, **b** 760ICHAZ, **c** 6ICHAZ, and **d** 7ICHAZ

Table 20.2 Grain orientation spread values and HAGB fraction for ICHAZ(s)

Grain orientation spread value (%)/sample	ICHAZ	760ICHAZ	6ICHAZ	7ICHAZ
Recrystallized [0–1.5]	69.3	48.3	59.0	69.8
Sub-structured [1.5–4]	30.7	51.4	40.3	30.2
Deformed [>4]	0.0	0.3	0.7	0.0
HABG [15–63°, %]	87.2	71.3	71.1	69.0

further decreased for deformed 760ICHAZ by increasing substructure. While re-normalizing and re-tempering with deformation further increased recrystallization by decreasing substructure of 760ICHAZ. It can be noted that this recrystallization value did not further decrease for 7ICHAZ rather than it increased by reducing substructure fraction. The presence of retained austenite in both ICHAZ and re-normalized 760ICHAZ transformed it into martensite in 760ICHAZ and 6ICHAZ, respectively. This transformation caused deformed grains in the latter samples. Table 20.2 also shows the values of HAGB, which confirmed that decreased HAGB in deformed 760ICHAZ was due to lath coarsening. This coarsening was constant in deformed 6ICHAZ. But, it slightly dropped for 7ICHAZ. During this characterization, it was observed that high deformed grains were present in ICHAZ followed by 760ICHAZ, 7ICHAZ, and 6ICHAZ.

20.3.2.3 Kernel Average Misorientation

Kernel average misorientation represents local strain distribution accumulated in microstructure [37] as shown in Fig. 20.6. Calculation of kernel average misorientation provides the average misorientation around the measured point with respect to the defined set of nearest neighbour points during EBSD. During kernel average misorientation calculation from EBSD data, the local misorientation was assigned to the centre point of any fixed grain with respect to all points in the perimeter of the kernel. Normally, the value of kernel average misorientation would be high in deformed grains due to a higher value of dislocation density. Also, the analysis of kernel average misorientation aids to understanding the localized deformation, local lattice distortions, and high dislocation density [38]. Furthermore, it qualitatively advises strain energy stored in a grain. The colour variation in kernel average misorientation maps depicts local strain distribution, i.e., blue colour represents no strain, whereas red represents highly strained region and green represents mild strain level. Therefore, the variation of colour in a kernel average misorientation map represents local strain distribution in the deformed microstructure of ICHAZ samples.

High values of kernel average misorientation were observed for 7ICHAZ followed 760ICHAZ and 6ICHAZ. Whereas, low values of kernel average misorientation existed in ICHAZ but they were more smoothly distributed in 6ICHAZ. High values of kernel average misorientation are attributed to the presence of carbide particles. In Fig. 20.6a, the heterogeneity was mainly observed around GBs. It means
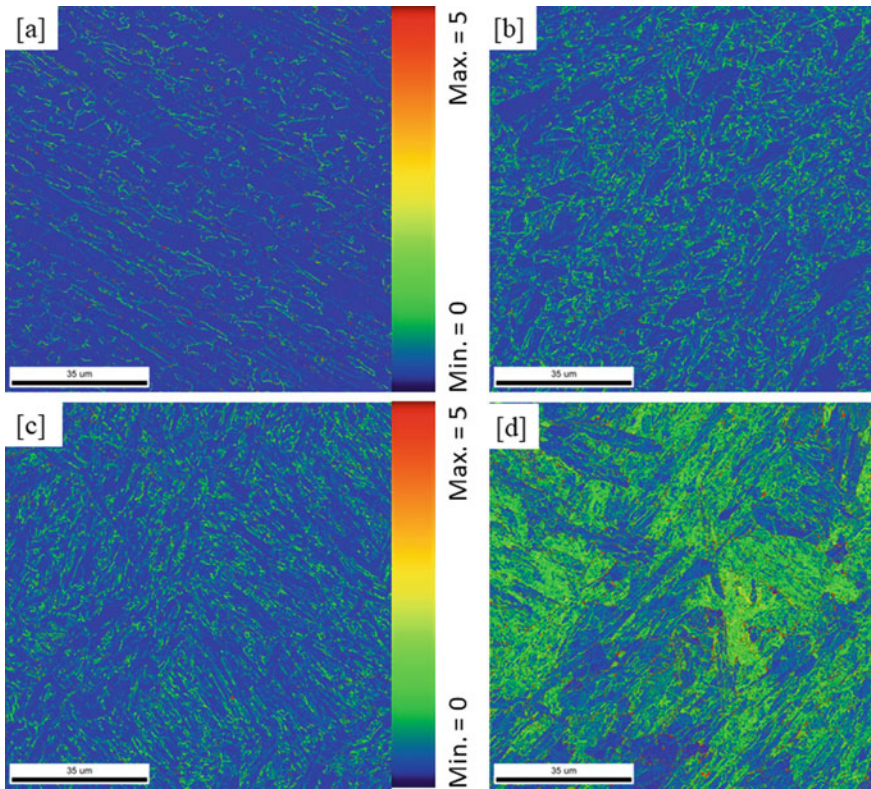
Fig. 20.6 Kernel average misorientation of **a** ICHAZ, **b** 760ICHAZ, **c** 6ICHAZ, and **d** 7ICHAZ

that carbides precipitated mainly at GBs, whereas in 760ICHAZ (Fig. 20.6b), heterogeneity was due to carbides formation both at GBs and inside the matrix. In both samples, owing to low values of kernel average misorientation after impression creep testing signified that de-alloying of matrix allowed higher creep deformation. The homogeneous kernel average misorientation distribution in 6ICHAZ confirmed that re-normalizing and re-tempering minimized heterogeneity in terms of refinement and softness by dissolving coarse carbides during re-normalizing that re-precipitated during re-tempering. This resulted in a delay in GB sliding during impression creep testing. However, the slight heterogeneity occurred during the second stage of tempering in 7ICHAZ. This was attributed to the high coarsening of carbides as notable in Fig. 20.6d.

20.4   Conclusions

Grain boundary hardening and softening effects of ICHAZ(s) were investigated by using impression creep testing and EBSD. Following conclusions were drawn from this study:

- Impression creep testing showed hardening in 6ICHAZ and 7ICHAZ while softening in ICHAZ and 760ICHAZ. In this respect, type IV cracking was absent for 6ICHAZ. The ratio of creep life for BM: ICHAZ: 760ICHAZ: 6ICHAZ: 760ICHAZ was 1: 0.004: 0.01: 1.05: 0.4, respectively.
- Less variation in boundary density as regards LAGB was found in ICHAZ, 760ICHAZ, and 6ICHAZ while slightly high values were observed 7ICHAZ. Whereas, boundary density as regards HAGB was higher in 7ICHAZ followed by ICHAZ and similar for the rest of ICHAZ(s).
- Higher recrystallization fraction was observed for ICHAZ and 7ICHAZ. This was less in 760ICHAZ and 6ICHAZ with an increasing sub-structured fraction. The presence of austenite caused high deformed fraction in 760ICHAZ and 6ICHAZ. HAGB was high in ICHAZ followed by 760ICHAZ, 6ICHAZ, and 7ICHAZ.
- High values of kernel average misorientation were present in 7ICHAZ followed by 760ICHAZ, 6ICHAZ, and ICHAZ. The homogeneity in kernel average misorientation among grains for 6ICHAZ caused hardening. While the degree of increased variation reduced hardening and invited softening.

References

1. Fujio, A., Kern, T.U., Viswanathan, R.: Creep-Resistant Steels. Elsevier (2008)
2. Khajuria, A., Kumar, R., Bedi, R.: Effect of boron addition on creep strain during impression creep of P91 steel. J. Mater. Eng. Perform. **28**(7), 4128–4142 (2019)
3. Laha, K., Chandravathi, K.S., Parameswaran, P., Rao, K.B.S., Mannan, S.L.: Characterization of microstructures across the heat-affected zone of the modified 9Cr-1Mo weld joint to understand its role in promoting type IV cracking. Metall. Mater. Trans. A **38**(1), 58–68 (2007)
4. Francis, J.A., Mazur, W., Bhadeshia, H.K.D.H.: Review type IV cracking in ferritic power plant steels. Mater. Sci. Technol. **22**(12), 1387–1395 (2006)
5. Abson, D.J., Rothwell, J.S.: Review of type IV cracking of weldments in 9–12% Cr creep strength enhanced ferritic steels. Int. Mater. Rev. **58**(8), 437–473 (2013)
6. Khajuria, A., Kumar, R., Bedi, R.: Characterizing creep behaviour of modified 9Cr1Mo steel by using small punch impression technique for thermal powerplants. J. mechan. Mechan. Engg. **4**(3), 47–61 (2018)
7. Akhtar, M., Khajuria, A., Kumar, V.S., Gupta, R.K., Albert, S.K.: Evolution of microstructure during welding simulation of boron modified P91 Steel. Phys. Met. Metallogr. **120**(7), 672–685 (2019)
8. Akhtar, M.: Metallurgical Characterisation of Simulated Heat Affected Zone in Boron Modified P91 Steel. National Institute of Technology, Warangal (2017)
9. Akhtar, M., Khajuria, A., Pandey, M.K., Ahmed, I.: Effects of boron modifications on phase nucleation and dissolution temperatures and mechanical properties in 9% Cr steels: sensitivity and stability. Mater. Res. Express **6**(12), 1265k1 (2019)

10. Akhtar, M., Khajuria, A., Kumar, R., Bedi, R.: Metallurgical investigations on dual heat cycled boron alloyed P91 ferritic/martensitic steel. In: Proceedings of Young Professionals Conference, International Institute of Welding, Chennai, India (2017). https://doi.org/10.13140/rg.2.2.18467.30241/2

11. Akhtar, M., Khajuria, A.: Probing true microstructure-hardening relationship in simulated heat affected zone of P91B steels. Metallogr. Microstruct. Anal. **8**(5), 656–677 (2019)

12. Akhtar, M., Khajuria, A.: Effects of prior austenite grain size on impression creep and microstructure in simulated heat affected zones of boron modified P91 steels. Mater. Chem. Phys. **249**, 122847 (2020)

13. Koisstinen, D.: A general equation prescribing the extent of the austenite-martensite transformation in pure iron-carbon alloys and plain carbon steels. Acta Metall. **7**, 59–60 (1959)

14. Akhtar, M., Khajuria, A., Pandey, M.K., Ahmed, I., Bedi, R.: Effects of boron modifications on phase nucleation and dissolution temperatures and mechanical properties in 9% Cr steels: alloy design. Mater. Res. Express **6**(12), 1265k3 (2019)

15. Maruyama, K., Kota, S., Jun-ichi, K.: Strengthening mechanisms of creep resistant tempered martensitic steel. ISIJ Int. **41**(6), 641–653 (2001)

16. Yan, W., Wang, W., Shan, Y., Yang, K., Sha, W.: 9–12Cr heat-resistant steels. Springer (2015)

17. Durand-Charre, M.: La microstructure des aciers et des fontes. SIRPE, Paris (2003)

18. Shi, P., Engström, A., Höglund, L., Sundman, B., Ågren, J.: Thermo-Calc and DICTRA enhance materials design and processing. Mater. Sci. Forum **475**, 3339–3346 (2005)

19. Goswami, P.: P(T) 91 steel—a review of current code and fabrication practices. In: Proceedings of the Sixth International Conference on Advances in Materials Technology for Fossil Power Plants, La Fonda, USA (2010)

20. Paul, V.T., Saroja, S., Vijayalakshmi, M.: Microstructural stability of modified 9Cr–1Mo steel during long term exposures at elevated temperatures. J. Nucl. Mater. **378**(3), 273–281 (2008)

21. Akhtar, M., Khajuria, A.: Probing true creep-hardening interaction in weld simulated heat affected zone of P91 steels. J. Manuf. Processes **46**, 345–356 (2019)

22. Abe, F., Tabuchi, M., Tsukamoto, S.: Alloy Design of Martensitic 9Cr-boron steel for A-USC boiler at 650°C-Beyond grades 91, 92 and 122. Energy Mater **2014**, 129–136 (2014)

23. Abe, F., Tabuchi, M., Kondo, M., Tsukamoto, S.: Suppression of Type IV fracture and improvement of creep strength of 9Cr steel welded joints by boron addition. Int. J. Press. Vessels Pip. **84**(1–2), 44–52 (2007)

24. Akhtar, M., Khajuria, A., Sahu, J.K., Swaminathan, J., Kumar, R., Bedi, R., Albert, S.K.: Phase transformations and numerical modelling in simulated HAZ of nanostructured P91B steel for high temperature applications. Appl. Nanosci. **8**(7), 1669–1685 (2018)

25. Khajuria, A., Bedi, R., Kumar, R.: Investigation of impression creep deformation behaviour of boron modified P91 steel by high end characterization techniques. In: Manufacturing Engineering, pp. 137–150. Springer, Singapore (2019)

26. Akhtar, M., Khajuria, A., Kumar, V.S., Gupta, R.K., Albert, S.K.: Evolution of microstructure during welding simulation of boron modified P91 steel. Phys. Met. Met. Sci **120**(7), 731–745 (2019). https://doi.org/10.1134/S0015323019070052

27. Vaibhav, A., Khajuria, A., Akhtar, M., Singh, M.P., Kumar, A.: Effects of heat treatments on grain size and hardness of P91 and boron added P91 steels, Behind The Teacher's Desk (BTTD-2017), CSIR-NML, Jamshedpur. India (2017). https://doi.org/10.13140/RG.2.2.20792.03841

28. Pal, S., Khajuria, A., Akhtar, M.: Influence of aging on hardness and tool wear of artificially aged aluminium alloy 6061. IAETSD J. Adv. Res. Appl. Sci. **5**(2), 477–481 (2018). http://iaetsdjaras.org/gallery/7-february-488.pdf

29. Huysmans, S., Vekeman, J., Hautfenne, C.: Dissimilar metal welds between 9Cr creep strength enhanced ferritic steel and advanced stainless steels—creep rupture test results and microstructural investigations. Weld. World. **61**(2), 341–350 (2017)

30. Hyde, T.H., Yehia, K.A., Becker, A.A.: Application of the reference stress method for interpreting impression creep test data. Mater. High Temp. **13**, 133–138 (1995). https://doi.org/10.1080/09603409.1995.11689511

31. Chu, S.N.G., Li, J.C.M.: Impression creep; a new creep test. J. Mater. Sci. **12**, 2200–2208 (1977). https://doi.org/10.1007/BF00552241

32. Khajuria, A., Akhtar, M., Kumar, R., Swaminanthan, J., Bedi, R., Shukla, D.K.: Effect of boron modified microstructure on impression creep behaviour of simulated multi-pass heat affected zone of P91 steel. In: Dutta, S., Chakraborty, S.S. (eds.) In: National Conference on Advanced Materials, Manufacturing and Metrology, pp. 150–157. CSIR-CMERI, Durgapur (2018). https://doi.org/10.13140/rg.2.2.34633.24164/2

33. Yu, H.-Y., Li, J.C.M.: Computer simulation of impression creep by the finite element method. J. Mater. Sci. **12**, 2214–2222 (1977). https://doi.org/10.1007/BF00552243

34. Chu, S.N.G., Li, J.C.M: Impression creep of β-tin single crystals. Mater. Sci. Eng. **39**, 1–10 (1979). https://doi.org/10.1016/0025-5416(79)90164-2

35. Talari, M.K., Kishore, B. N., Kallip, K., Leparoux, M., Koller, R.E., Alogab, K.A., Maedar, X.: Microstructure, mechanical, and impression creep properties of AlMg5–0.5 vol% Al2O3 nanocomposites. Adv. Eng. Mater. **18**, 1958–1966 (2016). https://doi.org/10.1002/adem.201600301

36. Dorner, D., Röller, K., Skrotzki, B., Stöckhert, B., Eggeler, G.: Creep of a TiAl alloy: a comparison of indentation and tensile testing. Mater. Sci. Eng., A **357**, 346–354 (2003). https://doi.org/10.1016/S0921-5093(03)00205-3

37. Wright, S.I., Nowell, M.M., Field, D.P.: A review of strain analysis using electron backscatter diffraction. Microsc. Microanal. **17**(3), 316–329 (2011)

38. Saraf, L.: Kernel average misorientation confidence index correlation from FIB sliced Ni-Fe-Cr alloy surface. Microsc. Microanal. **17**(S2), 424–425 (2011)